A numerical investigation of the evaporation process of a liquid droplet impinging onto a hot substrate

N. Nikolopoulos [a], A. Theodorakakos [b], G. Bergeles [a],*

[a] Department Mechanical Engineering, National Technical University of Athens, 5 Heroon Polytechniou, 15710 Athens, Greece
[b] Fluid Research, Co, Greece

Abstract

A numerical investigation of the evaporation process of *n*-heptane and water liquid droplets impinging onto a hot substrate is presented. Three different temperatures are investigated, covering flow regimes below and above Leidenfrost temperature. The Navier–Stokes equations expressing the flow distribution of the liquid and gas phases, coupled with the Volume of Fluid Method (VOF) for tracking the liquid–gas interface, are solved numerically using the finite volume methodology. Both two-dimensional axisymmetric and fully three-dimensional domains are utilized. An evaporation model coupled with the VOF methodology predicts the vapor blanket height between the evaporating droplet and the substrate, for cases with substrate temperature above the Leidenfrost point, and the formation of vapor bubbles in the region of nucleate boiling regime. The results are compared with available experimental data indicating the outcome of the impingement and the droplet shape during the impingement process, while additional information for the droplet evaporation rate and the temperature and vapor concentration fields is provided by the computational model.
© 2006 Elsevier Ltd. All rights reserved.

Keywords: Droplet evaporation; Volume of Fluid Method; Kinetic theory; Leidenfrost temperature

1. Introduction

The liquid–vapor phase change process, plays a significant role in a number of technological applications in combustion engines, cooling systems or refrigeration cycles. In all the aforementioned applications, the dynamic behavior of the impinging droplets and the heat transfer between the liquid droplets and the hot surfaces are important factors, which affect the mass transfer associated with liquid–vapor phase change.

The mechanism of the droplet spreading and the accompanying heat transfer is governed not only by non-dimensional parameters as the droplet Weber (*We*), the Reynolds (*Re*) number, Eckert (*E$_c$*) number, and Bond (*Bo*) number, but also by the temperature of the surface. As the droplet impacts upon the hot solid surface, heat is transferred from the solid to the liquid phase. This energy transfer to the droplet increases its mean temperature, while liquid vaporizes from the bottom of the droplet. If the heat transfer rate is large enough during the impact, liquid vaporized from the droplet forms a vapor layer between the solid and the liquid phase, which repels the droplet from the solid surface. In this case the heat transfer reaches a local minimum and the evaporation lifetime of the droplet becomes maximum. This phenomenon was first observed by Leidenfrost [1] in 1756 and hence the behavior is known as the Leidenfrost phenomenon. Based on the evaporation lifetime of a droplet, mainly four different evaporation regimes can be identified depending on the wall temperature; film evaporation, nucleate boiling, transition boiling and film boiling. This work contributes to the study of transition and film boiling impact regimes only.

* Corresponding author. Tel.: +30 2107721058; fax: +30 2107723616.
  E-mail addresses: niknik@fluid.mech.ntua.gr (N. Nikolopoulos), andreas@fluid-research.com (A. Theodorakakos), bergeles@fluid.mech.ntua.gr (G. Bergeles).

Nomenclature

Bo	Bond number, $(= \rho_{liq} g D_o^2 / \sigma)$
C_p	non-dimensional pressure, $\left(= \Delta P / \frac{1}{2} \rho_{liq} U_o^2\right)$
c_p	heat capacity (J/kg K)
D_{AB}	diffusivity of gas A to gas B, $(= \mu/(Sc \cdot \rho))$
E_c	Eckert number, $(= U_o^2 / (c_p (T_{liq} - T_w)))$
D_o	initial diameter of droplet
E_{sur}	surface energy
E_{kin}	kinetic energy
k	thermal conductivity (W/mK), $(= c_p \cdot \mu / Pr)$
MB	molecular weight (kg/kmol)
$\vec{n}$	vector normal to interface of the two phases
Oh	Ohnesorge number, $(= \mu_{liq}/(\sigma \rho_{liq} D_o)^{0.5})$
P	pressure
Pr	Prandtl number, $(= \mu c_p / k)$
$\overline{R}$	universal gas constant (J/kmol K)
R	computational radius
R_o	radius of initial droplet
Re	Reynolds number $(= \rho_{liq} D_o U_o / \mu_{liq})$
Sc	Schmidt number $(= \mu/(\rho D_{AB}))$
SYG	vapor concentration (mass of vapor (kg)/mass of gas phase (kg))
T	temperature
t	time
$\vec{T}$	stress tensor
$\vec{u}$	velocity
U_o	initial velocity of droplet

U_1	velocity of an equivalent droplet of the ring
V	volume
X	X-axis of computational field
Y	Y-axis of computational field
Z	Z-axis of computational field
Z_h	height of spreading droplet
We	Weber number, $(= \rho_{liq} D_o U_o^2 / \sigma)$

Greek symbols

α	volume of fluid (also noted as indicator function)
δ	vapor height
κ	curvature (m^{-1})
μ	dynamic viscosity
ρ	density
σ	surface tension
$\bar{\sigma}$	thermal accommodation coefficient

Subscripts

gas	gas phase
liq	liquid phase
b	base
vap	vapor
cell	computational cell
sat	saturation point
w	substrate or wall

The collision dynamics of a liquid droplet impinging on a hot surface has been investigated mainly experimentally. Researchers have presented a sequence of photographs showing the deformation process of liquid droplets impacting on a hot surface. Wachters and Westerling [2] were among the first to investigate the impact of a saturated water droplet of about 2 mm in diameter impinging on a polished gold surface heated to 400 °C, while Akao et al. [3] inspected the deformation behavior of various liquid droplets of 2 mm diameter on a chromium-plate copper surface heated to the same temperature. Xiong and Yuen [4] measured the time history of a *n*-heptane droplet impinging on a stainless-steel surface heated to temperatures between 63 °C and 605 °C. Chandra and Avedisian [5] performed the same experiment with a temperature range from 24 °C to 205 °C keeping a constant Weber number $We = 43$ while the same authors in [6] have presented results for the deformation process of a droplet impinging onto a porous ceramic surface. Naber and Farrell [7] examined the deformation process of liquid droplets of 0.1–0.3 mm in diameter impinging on a hot stainless-steel surface, while at the same time Anders et al. [8] investigated the rebounding phenomenon of ethanol droplets impacting obliquely on a smooth chromium-plated copper surface at 500 °C.

Ko and Chumg [9] investigated experimentally the effect of wall temperature on the break-up process of *n*-decane fuel, in the Leidenfrost temperature range of 220–330 °C, and demonstrated that wall temperature variation shows a peculiar nonlinear behavior in the droplet break-up probability, especially near 250 °C, which corresponds to the temperature of local maximum droplet lifetime. Manzello and Yang [10] examined the effect of an additive in a water droplet on its collision dynamics on a stainless-steel surface with the wall temperature varying from film evaporation to film boiling regime for three *Weber* number impacts.

Bernardin et al. [11,12] realizing that the impact parameters can alter the collision outcome, conducted a thorough series of experiments, concerning water droplets impinging on a polished aluminium surface, with the main controlling parameters of the phenomenon being droplet velocity, resulting in We number from 20 to 220 and surface temperature from 100 °C to 280 °C. They constructed droplet impact regime maps, which distinguish between the various boiling regimes for each of the three experimental We numbers investigated. Moreover, the heat flux from the surface was measured, for different We numbers, drop impact frequency and surface temperature, determining the two very important points in the regime map, the Leidenfrost point (LFP) and the critical heat flux point (CHF). The first

corresponds to the minimum heat flux point and the second to the lower temperature boundary of the transitional boiling regime.

Apart from the above-mentioned controlling parameters for the description of such a phenomenon, secondary parameters such as surface roughness, control the evolution of this phenomenon. Most of the researchers ignored the effects of surface roughness on droplet heat transfer. Cumo et al. [13], Baumeister et al. [14] and Nishio and Hirata [15] observed that rough surfaces require a thicker vapor layer between the droplet and the surface to sustain film boiling and, therefore, possess a higher LFP temperature. Avedisian and Koplik [16] found that the LFP for water droplets on porous ceramic surfaces increases with increasing porosity. Engel [17] observed that surface roughness promotes droplet break-up, and Ganic and Rohsenow [18] reported surface roughness enhances liquid–solid contact in dispersed droplet flow and hence increases film boiling heat transfer. Fujimoto and Hatta [19] and Hatta et al. [20] confirmed that the critical *We* number, above which whether or not the droplet is disintegrated during deformation, depends on the kind of surface material. Wachters and Westerling [2] observed experimentally that the critical *We* number, above which disintegration of a droplet impinging on a hot wall once the droplet is transformed into an expanding torus is around 80.

Bernardin et al. [11,12] used three different surface finishes and reported that although the temperature corresponding to the critical heat flux (CHF) was fairly independent of surface roughness, the Leidenfrost point (LFP) temperature was especially sensitive to surface finish. They produced regime maps illustrating not only the well-known boiling curve regimes of liquid film, transition and nucleate boiling, but also the complex liquid–solid interactions which occur during the lifetime of the impacting droplet.

One more important secondary controlling parameter, essential not only for the description of physics of this phenomenon, but also for its numerical simulation, is the value of contact angles. Bernardin et al. [11,12] using the sessile drop technique measured the variation of contact angles for an aluminum surface, as a function of surface temperature, while Chandra et al. [21] studied the effect of contact angles on droplet evaporation, adding varying amounts of a surfactant to water.

A few studies have examined the effect of reduced gravity. Siegel [22] has reviewed much of the work done on this topic. The principal findings were that gravity has little effect on the nucleate pool boiling heat transfer coefficients. For low wall heat flux, vapor bubble diameters increase at low gravity. Furthermore, the critical heat flux decreases in the absence of buoyancy forces while stable film boiling can be maintained at low gravity, but heat transfer is reduced. Qiao and Chandra [23] performed a series of experiments, using water and *n*-heptane, intending to isolate the effect of buoyancy forces on droplet impact and boiling. Their objective was to study the effect of gravity and liquid properties on transition from nucleate to film boiling.

Due to the highly complex nature of these processes, development of methods to predict the associated heat and mass transfer has often proved to be a difficult task. Nevertheless, research efforts over several decades have provided an understanding of many aspects of vaporization or condensation. Important and interesting numerical simulations of droplet collisions with a variety of methods have also been published. The MAC-type solution method to solve a finite-differencing approximation of the Navier–Stokes equations governing an axisymmetric incompressible fluid flow was used by Fujimoto and Hatta [19] and Hatta et al. [20]. The simulation of the flow field inside the liquid droplet has been performed assuming a simple thermal distribution such that temperature becomes lower (higher) on the upper (lower) side of the droplet and higher with time. The unsteady thermal distribution inside the droplet is not calculated, assuming the temperature of the droplet's bottom to be at the saturation temperature and that a vapor layer exists between the droplet and solid surface.

A number of analytical studies by Gottfried et al. [24], Wachters et al. [25], Nguyen and Avedisian [26], and Zhang and Gogos [27] are dealing with the Leidenfrost phenomenon and the steady-state droplet film boiling. Indispensable condition for these studies is that the droplet has a nearly steady spherical shape, so that the heat transfer rates and droplet evaporation times can be predicted successfully.

Pasandideh et al. [28] used a complete numerical solution of the Navier–Stokes and energy equations, based on a modified SOLA-VOF method, to model droplet deformation and solidification, including heat transfer in the substrate. The heat transfer coefficient at the droplet-substrate interface was estimated by matching numerical predictions of the variation of substrate temperature with measurements. Heat transfer in the droplet was modeled by solving the energy equation, neglecting viscous dissipation, whilst the effect of substrate's cooling on the droplet's evaporation was taken into account [29]. Following that, Pasandideh et al. [30], extended the model developed by Bussmann et al. [31] and combined a fixed-grid control volume discretization scheme of the flow and energy equations with a volume tracking algorithm to track the droplet free surface. Surface tension effects were also taken into account. The energy equation both in the liquid and solid portion of the droplet were solved using the Enthalpy method in the case of solidification. More recent three-dimensional codes have been used to model complex flows such as impact on inclined surfaces resulting in droplet break-up, as shown by Zheng and Zhang [32] and splashing, according to Ghafouri-Azar et al. [33]. Zheng and Zhang [32] developed an adaptive level set method for moving boundary problems in the case of droplet spreading and solidification.

Zhao and Poulikakos [34,35] studied numerically the fluid dynamics and heat transfer phenomena both in droplet and the substrate, based on the Lagrangian formulation and utilizing the finite element method in a deforming

mesh. The temperature fields developing in both the liquid droplet and the substrate during the impingement process were also determined. Waldvogel and Poulikakos [36] followed the Langrangian formulation including surface tension and heat transfer with solidification. They investigated the effect of initial droplet temperature, impact velocity, thermal contact resistance and initial substrate temperature on droplet spreading, on final deposit shapes and on the times to initiate and complete freezing. Butty et al. [37] solved the energy equation in both the droplet and substrate domain, implementing a time and space averaged thermal contact resistance between the two thermal domains. During calculations a regeneration of mesh technique is used, in order to enhance accuracy. Harvie and Fletcher [38–40] coupled VOF methodology with a separate one-dimensional algorithm to model not only the hydrodynamic gross deformation of the droplet, impacting onto a hot wall surface, but also the fluid flow within the viscous vapor layer existing between the droplet and the solid surface. The height of the vapor layer was assumed to be several orders of magnitude smaller than the dimensions of the droplet, resulting in a Knudsen number approaching values of the order of 0.1. It is important to note that the height of the vapor layer does not result from the solution of the Navier–Stokes equations, but it was assumed to be known. Furthermore, they used a kinetic theory treatment in order to calculate conditions existing at the non-equilibrium interface of the vapor layer, solving the heat transfer within the solid, liquid and vapor phases. This model was validated for a number of droplet impact conditions, covering a wide range of *We* numbers and initial droplet and surface temperatures.

The present investigation studies numerically the impingement of *n*-heptane and water droplets on a hot substrate under various temperatures, covering regimes above and below the Leidenfrost temperature. Viscous dissipation and surface tension effects are taken into account; the equations are solved numerically with the finite volume methodology, whilst the Volume of Fluid methodology of Hirt and Nichols [41] is used for the tracking of the liquid–gas interface. The methodology is coupled with an adaptive local grid refinement technique, both in 2-D axisymmetric and fully three-dimensional cases, allowing the prediction of details of droplet's levitation, above the Leidenfrost temperature, without any 'a priori' assumption for the vapor layer height. Moreover in contrast to other methodologies, in the case of impact below the Leidenfrost point, the entrapment of vapor between the liquid droplet and the wall is predicted, The evaporation model coupled with VOF methodology is used in an in-house developed CFD code, predicting not only the deformation of the liquid droplet and the height of vapor blanket in the case of the above Leidenfrost temperature, but also the corresponding temperature and vapor fields. The used model is validated for a number of droplet impacts both for low and high *We* numbers and substrate temperatures. The heat transfer inside the substrate is not solved, as the substrate tempera-

ture is considered to be constant, the liquid–gas interface is assumed to be at saturation conditions, whilst the effect of substrate roughness on the droplet spreading is not taken into account.

2. The numerical solution procedure

2.1. Fluid flow

The flow induced by the impact of a droplet on a hot surface, is considered as two-dimensional axisymmetric for cases A, B, and C (*n*-heptane) and for case D (water) as three-dimensional; the details of the test conditions investigated are summarized in Table 1. The volume fraction, denoted by α, is introduced following the Volume of Fluid Method (VOF) of Hirt and Nichols [41] in order to distinguish between the gas and the liquid phases. This is defined as:

$$\alpha = \frac{\text{Volume of liquid phase}}{\text{Total volume of the control volume}} \quad (1)$$

where the α-function is equal to:

$$a(x,t) = \begin{cases} 1, & \text{for a point } (x,t) \text{ inside liquid phase} \\ 0, & \text{for a point } (x,t) \text{ inside gas phase} \\ 0 < \alpha < 1, & \text{for a point } (x,t) \text{ inside the transitional} \\ & \text{area between the two phases} \end{cases} \quad (2)$$

For a single droplet splashing onto a wall film, the VOF methodology has been successfully applied and the method is described in more detail in Nikolopoulos et al. [42].

The momentum equation is written in the form:

$$\frac{\partial(\rho\vec{u})}{\partial t} + \nabla \cdot (\rho\vec{u} \otimes \vec{u} - \vec{T}) = \rho\vec{g} + \vec{f}_\sigma \quad (3)$$

where $\vec{T}$ is the stress tensor, $\vec{u}$ is the velocity, ρ is the density of the mixture and f_σ is the volumetric force due to surface tension. The value of f_σ is equal to $f_\sigma = \sigma \cdot \kappa \cdot (\nabla a)$, where σ is the numerical value of the surface tension (for immiscible fluids the value is always positive) and κ is the curvature of the interface region.

The flow field is solved numerically on two or three-dimensional unstructured grids, using a recently developed adaptive local grid refinement technique, following the finite volume approximation, coupled with the VOF methodology; a detailed discussion of the fluid flow model is presented by Nikolopoulos et al. [42], while the adaptive local grid refinement technique is used in order to enhance accuracy of the predictions in the areas of interest (i.e. the liquid–gas interface), with minimum computational cost, as shown by Theodorakakos and Bergeles [43]. To account for the high flow gradients near the free surface, the cells are locally subdivided to successive resolution levels, on both sides of the free surface. As a result, the interface is

Table 1
Test cases examined

Case	A	B	C	D
Liquid	*n*-Heptane	*n*-Heptane	*n*-Heptane	Water
R_o	0.00075	0.00075	0.00075	0.0015
U_o	0.8	0.8	0.8	2.34
We	34.52	34.52	34.52	222.10
Re	2156.09	2156.09	2156.09	7638.78
Oh	0.00273	0.00273	0.00273	0.00195
Bo	0	0	0	1.19
E_c	0.034	0.031	0.028	0.060
T_w (°C)	178	190	210	180
T_{liq} (°C)	25	25	25	27
Computational domain $(X_{tot}, Y_{tot}, Z_{tot})$	$13.33R_o \times 6.67R_o$	$13.33R_o \times 6.67R_o$	$13.33R_o \times 6.67R_o$	$10R_o \times 10R_o \times 6.67R_o$
Base grid	60×30 (4 levels local refinement)	60×30 (4 levels local refinement)	60×30 (4 levels local refinement)	$45 \times 45 \times 30$ (3 levels local refinement)
Maximum number of grid nodes	11314	16353	13183	499132

always enclosed by the densest grid region. A new locally refined mesh is created every 20 time steps for the cases that will be presented afterwards. The numerical cell at which subdivision is performed, is locally refined by a factor of 3 for case D or 4 for cases A, B, and C (i.e. in two dimensions an initial cell is split into four cells). In that way a new grid with 1 level of local refinement is created. Obviously, computations are more time efficient on the dynamically adaptive grid, than on the equivalent fine resolution uniform grid.

The high-resolution differencing scheme CICSAM, proposed by Ubbink and Issa [44] in the transport equation for α (VOF-variable) is used. The discretization of the convection terms of the velocity components is based on a high resolution convection-diffusion differencing scheme (HR scheme) proposed by Jasak [45]. The time derivative was discretized using a second-order differencing scheme (Crank–Nicolson). Quadrangular (2D) or hexahedron (3D) computational cells are used. Finally, the contact angles at the advancing and receding contact lines are assigned as boundary conditions.

2.2. Heat transfer

Heat transfer in the droplet was predicted by solving the energy equation, calculating all physical properties as a function of the corresponding properties of the liquid and gas (air and vapor) phase. Such properties are density, viscosity, heat capacity and Prandtl number. All properties were assumed to vary with temperature and pressure, including the diffusivity of vapor in air (D_{AB}). The surface tension coefficient is assumed to vary also with temperature.

Heat transfer within the liquid phase is described by the following thermal energy transport equation (enthalpy equation) for incompressible fluids:

$$\rho \frac{\mathrm{D}h'}{\mathrm{D}t} = \nabla(k \cdot \nabla T) + \frac{\mathrm{D}P}{\mathrm{D}t} + \dot{Q}, \tag{4}$$

In this equation, $\dot{Q}$ is a source term due to evaporation and is equal to the amount of heat released, when liquid passes through the liquid–vapor interface and evaporates:

$$\dot{Q} = \left(\frac{\mathrm{d}m/\mathrm{d}t}{V_{cell}} \right) \cdot L, \quad L = (C_{p,liq} - C_{p,vap}) \cdot T, \tag{5}$$

where L is the latent heat of vaporization of liquid and $\mathrm{d}m/\mathrm{d}t$ the evaporation rate of the liquid phase.

The value of $\dot{Q}$ term is proportional to the mass flux of liquid molecules which evaporate. Following Langmuir's [46] approach, whereby the liquid and vapor phases are assumed to be separated by a discrete molecular layer, but including the Schrage's correction [47] to account for molecular flow towards or away from the liquid surface, the evaporated mass flux is equal to

$$\mathrm{d}m/\mathrm{d}t = \left[\frac{2 \cdot \bar{\sigma}}{2 - \bar{\sigma}} \right] \cdot \left(\frac{MB_{vap}}{2 \cdot \pi \cdot \bar{\bar{R}}} \right)^{1/2} \cdot \left(\frac{P_{sat,liq}}{T_{liq}^{1/2}} - \frac{P_{sat,vap}}{T_{vap}^{1/2}} \right) > 0 \tag{6}$$

where $\bar{\sigma}$ is the thermal accommodation coefficient.

It seems that thermal accommodation coefficient has not been measured with any real confidence yet, but its value is in the range of 0–1. Here, a value of 0.5 has been chosen both for *n*-heptane and water.

Apart from the energy equation, an additional transport Eq. (7) for the concentration of vapor in the gas is solved

$$(1 - \alpha) \cdot \rho_{air} \frac{\mathrm{D}C}{\mathrm{D}t} = \nabla[(1 - \alpha) \cdot \rho_{air} \cdot D_{AB} \cdot \nabla C] + \left(\frac{\mathrm{d}m/\mathrm{d}t}{V_{cell}} \right) \tag{7}$$

where C is the concentration of the vapor phase in the gas phase (kg_{vapor}/kg_{gas}). For the mixed phase of liquid and gas, physical and thermodynamic properties are calculated

as a function of α (volume fraction α), using linear interpolation between the values of the two phases:

$$\rho = \alpha\rho_{\text{liq}} + (1 - \alpha)\rho_{\text{gas}}$$
$$\mu = \alpha\mu_{\text{liq}} + (1 - \alpha)\mu_{\text{gas}} \tag{8}$$
$$Pr = \alpha Pr_{\text{liq}} + (1 - \alpha)Pr_{\text{gas}}$$

However, in the case of heat capacity, which has units of J/(kg K), a mass and not volume weighted interpolation is used in every computational cell, i.e.

$$C_p = \frac{m_{\text{liq}}}{m_{\text{tot}}} \cdot C_{p,\text{liq}} + \left(1 - \frac{m_{\text{liq}}}{m_{\text{tot}}}\right) \cdot C_{p,\text{gas}}$$
$$C_{p,\text{gas}} = \frac{m_{\text{vap}}}{m_{\text{gas}}} \cdot C_{p,\text{vap}} + \left(1 - \frac{m_{\text{vap}}}{m_{\text{gas}}}\right) \cdot C_{p,\text{air}} \tag{9}$$
$$= C \cdot C_{p,\text{vap}} + (1 - C) \cdot C_{p,\text{air}}$$

while the masses are calculated as:

$$m_{\text{liq}} = \alpha \cdot \rho_{\text{liq}} \cdot V_{\text{cell}}$$
$$m_{\text{vap}} = (1 - \alpha) \cdot C \cdot \rho_{\text{gas}} \cdot V_{\text{cell}}$$
$$\rho_{\text{gas}} = \frac{P}{\frac{\bar{R}}{MB_{\text{gas}}} \cdot T},$$
$$MB_{\text{gas}} = x \cdot MB_{\text{vap}} + (1 - x) \cdot MB_{\text{air}}, \quad x\text{-molar fraction} \tag{10}$$

where x is the molar fraction of vapor in the gas phase

$$x = \frac{\frac{C}{MB_{\text{vap}}}}{\frac{C}{MB_{\text{vap}}} + \frac{1-C}{MB_{\text{air}}}} \tag{11}$$

It should be mentioned that the kinetic theory of evaporation applies only when a gas/liquid interface exists. In the regions where contact between the liquid droplet and the hot substrate exists, no evaporation is calculated.

3. Numerical details

The value of the thermal accommodation coefficient is assumed to be equal to 0.5, since no other reference for these cases has been reported in the literature. Following Langmuir's [46] approach, the interface of the droplet is assumed to be at saturation conditions, and the vapor phase immediately adjacent to it. Substrate's cooling is not taken into account, since its temperature is supposed to be constant. According to Chandra et al. [21] and Pasandideh et al. [29] the substrate's cooling increases, reducing the static contact angle of the liquid droplet, resulting in a maximum cooling at around 20 K, when the droplet is totally evaporated. Finally, the effect of substrate's roughness on the spreading of the liquid droplet upon it is not taken into account. However, specifically for case C, neglecting substrate's cooling is not affecting the evolution of the phenomenon, since the droplet levitates over it.

The hydrodynamic and thermodynamic characteristics of the impact of a single droplet onto a hot solid surface

depend on the characteristics of the impinging droplet i.e. droplet diameter D_o, initial droplet velocity U_o, on the physical properties of the liquid and gas phase i.e. viscosity μ, density ρ, surface tension σ, and also on the substrate temperature T_w.

During the impact of the droplet onto a hot substrate, depending on the substrate temperature, the droplet may experience different heat transfer regimes of the boiling curve such as: (a) natural convection, (b) nucleate boiling, (c) transition boiling and (d) film boiling. Depending on the *We* number, droplets may either spread on the surface and then rebound (low *We* number, *We* < 30), or spread on the surface but then, upon shrinking and rebounding droplets split into a large globule and a small spherical droplet (intermediate *We* number, 30 < *We* < 80). Finally, in the high *We* number regime (*We* > 80), the droplet spreads out radially into a flat disk, the rim of which breaks into several small droplets which quickly disperse away from the rim. The liquid film which is on the flat disk itself then breaks up into many small droplets.

As a consequence, parameters including the droplet Weber number (*We*), the Reynolds number (*Re*) or the Ohnesorge number (*Oh*), which is a combination of *We* and *Re* numbers, the Bond number (*Bo*) and the initial temperature both of droplet and substrate are introduced to describe the initial configuration of the phenomenon.

Both two and three-dimensional domains have been used, the liquid phase is *n*-heptane or water correspondingly and the gas phase is air under atmospheric pressure. The range of parameters for which computations have been performed, is given in Table 1.

In all cases the "base" grid employed consisted of 1800 cells in the 2-D axisymmetric and 60,750 in the 3-D case. Three and four levels of local refinement in the case 3-D and 2-D cases have been used, respectively, resulting in a maximum number 500,000 computational cells for the 3-D and 15,000 for the 2-D cases. The numerical simulation for the axisymmetric cases A, B and C, lasted for 1 1/2 days in a Pentium 4 2.4 GHz, while for case D computations lasted for 30 days. At the start of calculations and after grid refinement for the axisymmetric cases, the droplet is covered by 2300 cells, whilst 397 cells resolve the interface. In the three-dimensional case the droplet is covered by 35.626 cells while the interface is resolved by 6657 cells. Obviously, computations are more time efficient on the present dynamically adaptive grid, than on the equivalent fine resolution and uniform grid. Cases A, B and C would require equivalent to 460,505 and case D equivalent to 3,067,0623 number of cells of a uniform fine grid.

Case C is identical to that previously studied by Harvie and Fletcher [40] using 50 × 140 square cells over a computational domain of $9.33R_o \times 3.33R_o$. Cases A, B and C have been examined experimentally by Qiao and Chandra [23], in low gravity environment. Case D has been examined experimentally by Bernardin et al. [52]. In case D the hot substrate is located at plane $Z = 0$ and the gravity is pointed downwards; mirror boundary conditions that
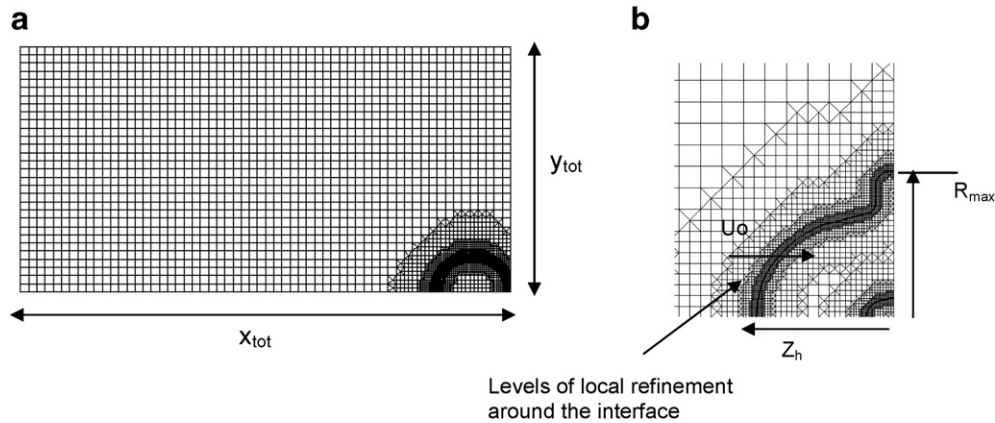
Fig. 1. (a) Numerical grid and (b) some basic global quantities concerning the spreading droplet.

allow the simulation of a droplet on the axis $X = Y = 0$ with fourfold symmetry are introduced.

The evaporation model is coupled with the VOF methodology. As a result, the vapor layer forming between the liquid and the solid surface can be predicted during the numerical solution without a need for 'a priori' assumption of its height. During the calculations, all hydrodynamic and thermodynamic coefficients including surface tension are a function of temperature. However, it should be noticed that the heat transfer inside the substrate is not solved, and the substrate's temperature is considered to be constant.

A typical form of the droplet's shape with the corresponding numerical grid just before impact is shown in Fig. 1a. Two dimensions are used to characterize droplet spreading as function of time: the radius of the wetted area, R_{max}, and the maximum droplet height above the surface Z_h. Fig. 1b shows schematically the definition of these parameters, which have been also investigated and reported in recent literature.

4. Presentation and discussion of the results

4.1. Time evolution of n-heptane droplet impingement

4.1.1. n-Heptane, $T_w = 178\,°C$ (case A)

The impact of n-heptane droplet on a hot stainless-steel at low gravity environment has been investigated experimentally by Qiao and Chandra [23]. Low gravity boiling experiments have shown that inertial and surface tension effects are sufficient to cause bubble creation during nucleate boiling, even in the absence of buoyancy, Siegel [22], Straub et al. [48], Oka et al. [49] and Ervin et al. [50]. As reported by Qiao and Chandra [23], the Leidenfrost temperature of n-heptane is 200 °C, which corresponds to its thermodynamic superheat limit, a property that is not affected by gravity. As a result, the conditions of this case correspond to low We number impact and as far as the heat map regime is concerned, it belongs to transition boiling.

Chandra and Avedisian [5] conducted experiments with n-heptane droplets impinging on stainless steel surface, and

reported a variation of contact angle between the liquid and the surface, as a function of surface's temperature. For $T_w=178\,°C$, this angle is equal to around 100°; this value has been incorporated into the numerical model.

Fig. 2a presents computational results at successive time steps, during droplet impingement for case A, at which Qiao and Chandra [23] present their experimental droplet shapes. The comparison between the predicted droplet shapes and the experimental ones is generally good. At the initial stages (Fig. 2a, $t = 0.2$ ms) of the impact, a small bubble of air close to the centre line between the droplet and the substrate is formed. At the same time, the droplet spreads radially roughly until $t = 4$ ms where it reaches its maximum spreading radius. Following, the liquid begins to shrink towards the axis of symmetry while at the same time its central part lifts up due to the effect of internal bubble growing. This is clear during the time period between $t = 4.95$–6.6 ms after impact. As can be seen in Fig. 2a, the numerical simulation predicts the initial spreading of the droplet on the surface (Fig. 2a, $t = 4$ ms), the shrinking and lifting of droplet, while the droplet remains in contact with the surface until $t = 13.6$ ms is reached. This behavior is also confirmed by the corresponding experimental data.

Since T_w is above the boiling point of n-heptane ($T_b = 98.4\,°C$) nucleate boiling occurs within in the contact surface between the surface and the droplet. The vapor bubbles grow from surface imperfections and cavities in which liquid and air are trapped, promoting heterogeneous nucleate boiling. An increasing number of surface nucleation sites are activated as temperature increases and the droplet evaporation time decreases with increasing T_w. For $T_w > 180\,°C$ the pressure of the vapor formed below the droplet increases enough to levitate the droplet and the bulk liquid mass makes only intermittent contact with the surface, as reported by Nishio and Hirata [51]. This is confirmed by the present numerical predictions, without need for use of any other empirical model for heterogeneous nucleate boiling. This can be seen in Fig. 2a. at time corresponding to $t = 4$ ms after impact. The bubbles present inside the droplet at the initial stages of the impact (Fig. 2a, $t = 0.2$ ms), merge together forming vapor slugs
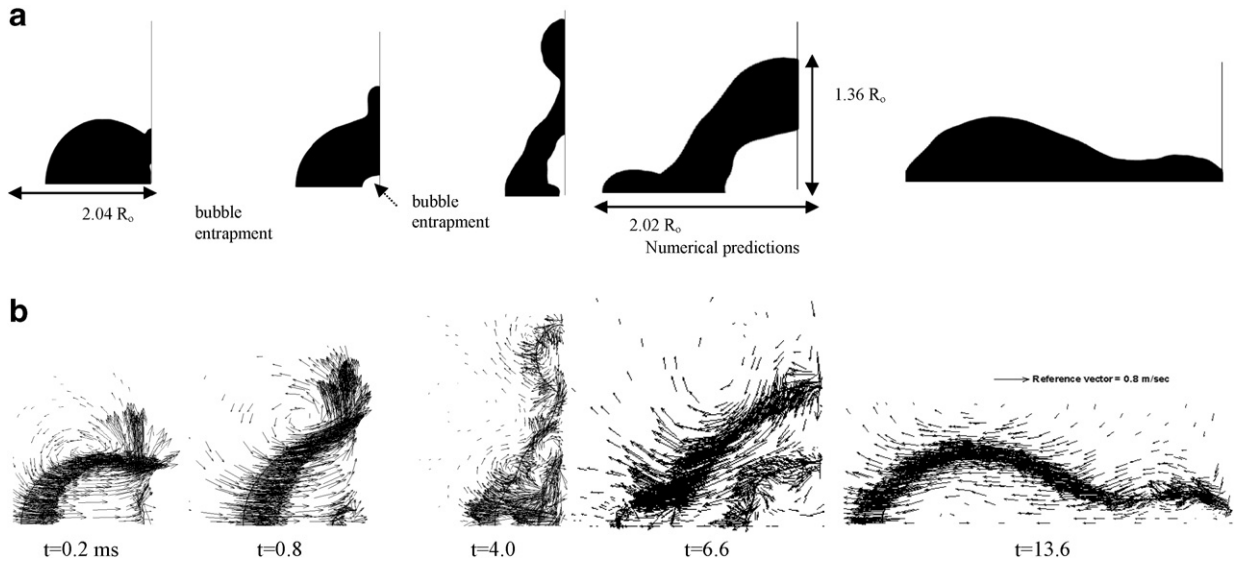
Fig. 2. (a) Droplet shape evolution for case A and (b) vector field ($We = 34.52$, $Re = 2156$, $T_w = 178\,°C$, $E_c = 0.034$).

that move upward (opposite to $\vec{U}_o$) inside the liquid and towards its surface (Fig. 2a, $t = 4.0$ ms). This mechanism forces the central part of the droplet to lift off from the heated surface, as can be seen in Fig. 2a during the time window between $t = 6.6$–13.6 ms.

The motion of the droplet towards the substrate induces a gas velocity field, in the form of a vortex ring attached to the droplet (Fig. 2b, $t = 0.2$, 0.8 ms). This vortex ring is always attached to the rim of the spreading droplet, (Fig. 2b, $t = 0.8$ ms), and at time 2.95 ms, when the droplet begins to shrink, changes its flow direction (Fig. 2b, $t = 4.0$ ms). The value of the maximum gas jetting velocity is approximately 444% of the droplet impact velocity, whilst the liquid jetting velocity is approximately 315% of the droplet impact velocity. Values of pressure up to approximately 1016% ($C_p = (P - P_{oo}(= 1\ \text{atm}))/(0.5\rho_{\text{liq}} U_{oo}^2)$) of the initial droplet kinetic energy during the initial stages of droplet impact appear at $t = 0.1$ ms (Fig. 3a and b), and a magnified view of the droplet base indicates that a vapor bubble is created between the droplet

and the substrate, while inside it a vortex ring of the gas phase exists (Fig. 3b and c).

In Fig. 4a and b the corresponding temperature and vapor fields at representative time instants are presented. Initially the temperature in the droplet area is lower due to droplet cooling effect, but latter the droplet is heated up, liquid evaporates and creates the expansion of the central bubble, Fig. 4a, $t = 13.6$ ms.

The bubble beneath the liquid is full of vapor due to evaporation, as can be seen in Fig. 4b at times between $t = 0.2$ ms and 4.0 ms, while the gas field around the droplet has less vapor concentration. At later stages when droplet rebounds, the vapor concentration around the lower-side part of the droplet increases, due to the convective transport of vapor from the droplet-substrate area, as can be seen in Fig. 4b at the time of $t = 13.6$ ms.

4.1.2. n-Heptane, $T_w = 190\,°C$ (case B)

Like in case A, case B is characterized by a low impact We number and it can be classified in the transition boiling
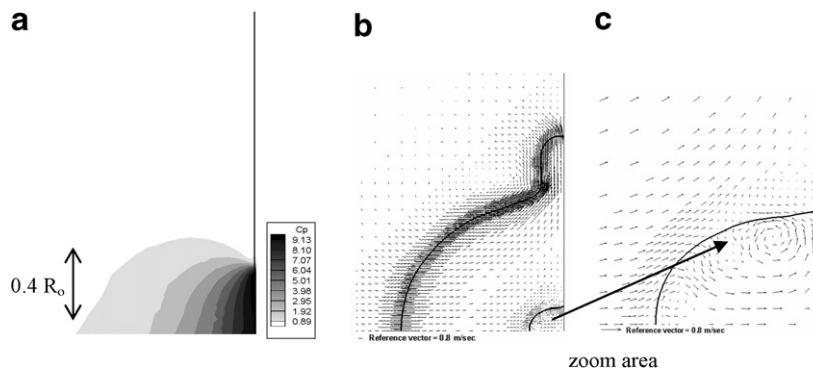
Fig. 3. (a) Pressure contour within the droplet at 0.1 ms, (b) velocity field at 0.8 ms and (c) zoom area inside the vapor bubble at 0.8 ms, for case A ($We = 34.52$, $Re = 2156$, $T_w = 178\,°C$, $E_c = 0.034$).
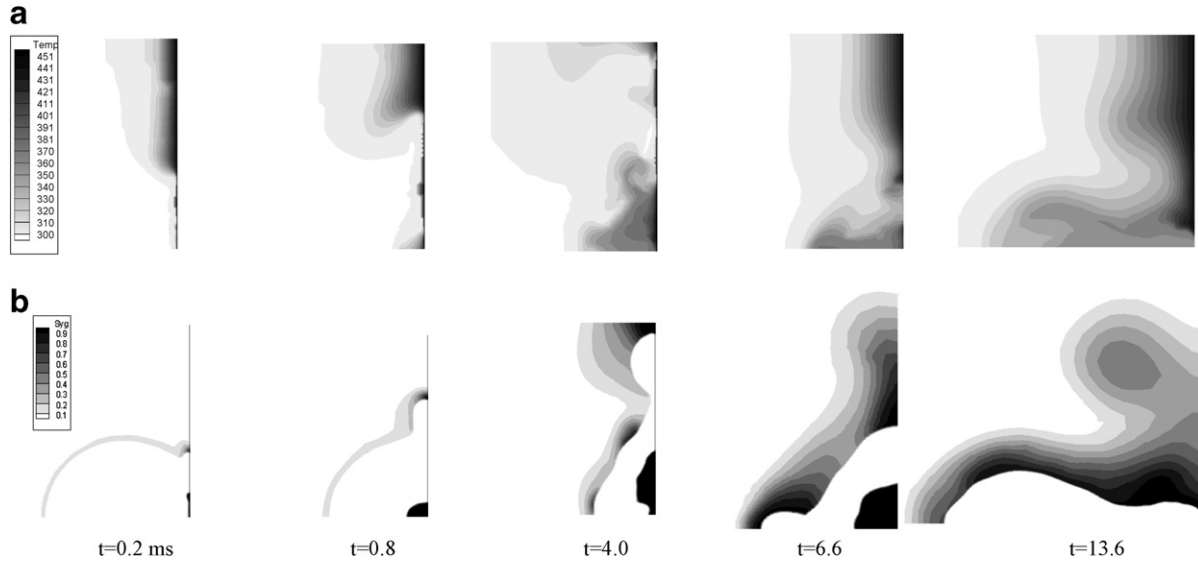
Fig. 4. (a) Temperature filed for case A, and (b) vapor concentration field ($We = 34.52$, $Re = 2156$, $T_w = 178$ °C, $E_c = 0.034$).

regime. For $T_w = 190$ °C, the contact angle is greater than in case A, and equals to around 120°. The numerical simulation of this phenomenon predicts, Fig. 5a, spreading of the droplet on the surface and then its rebound, which is confirmed by the corresponding experimental data. With increasing surface superheat, the evaporation rate is higher than in case A and the vapor bubble volume is larger; this is shown in Fig. 6b at $t = 4.0$ ms. The pressure difference force which the vapor bubble exerts on the liquid opposes liquid moving towards the surface; as a result, compared to case A lift off from the substrate is faster and at a higher level. The latter is confirmed both by the experimental and numerical results shown at $t = 6.6$ ms in Fig. 5a. At this time, the droplet almost lifts off from the substrate, while two satellite droplets are formed at its base. The percentage volume of these two small satellite droplets is equal

to 0.038% and 0.242% of the initial droplet's volume. At $t = 13.6$ ms, the droplet has lift-off at a distance almost $21/2$ R_o above the substrate's surface, while at the same time in the previously examined case A, it was still almost touching it.

The motion of the droplet towards the substrate induces a similar to case A gas velocity field, in the form of a vortex ring attached to the droplet, as shown in Fig. 5b at $t = 0.2$ and 0.8 ms. The values of the maximum gas jetting and liquid jetting velocity are approximately 496% and 317% of the droplet impact velocity, respectively. Values of pressure up to 2140% ($C_p = (P - P_{oo}(= 1 \text{ atm}))/(0.5\rho_{liq}U_{oo}^2)$) of the initial droplet kinetic energy during the initial stages of droplet impact are calculated. It is of interest also to note that both the maximum non-dimensional air and liquid jetting velocity are almost equal for both cases A
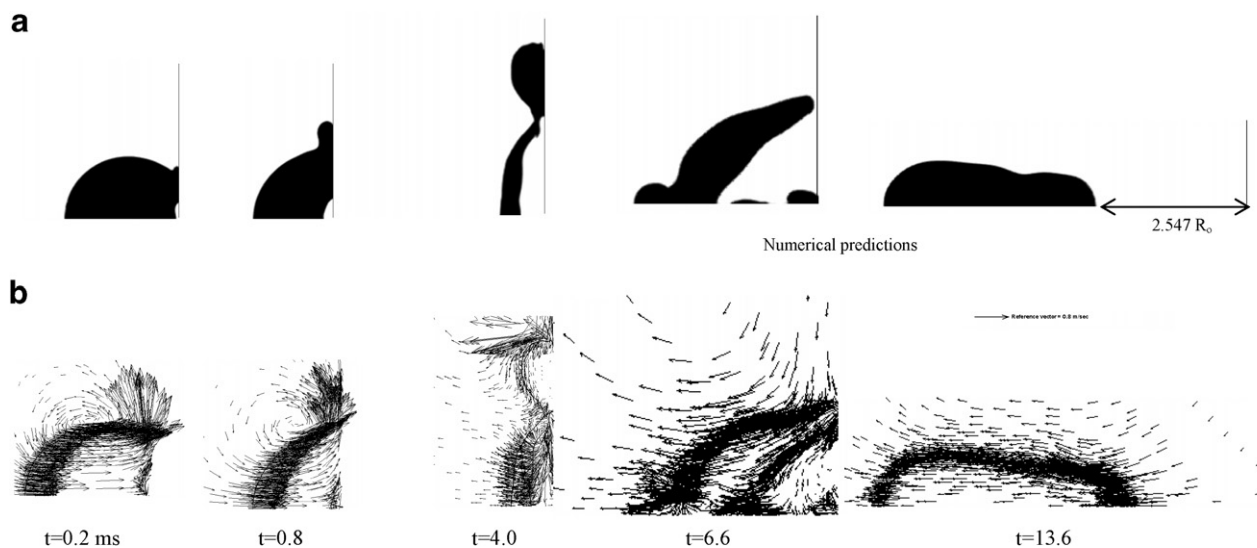
Fig. 5. (a) Droplet shape evolution for case B and (b) vector field ($We = 34.52$, $Re = 2156$, $T_w = 190$ °C, $E_c = 0.034$).
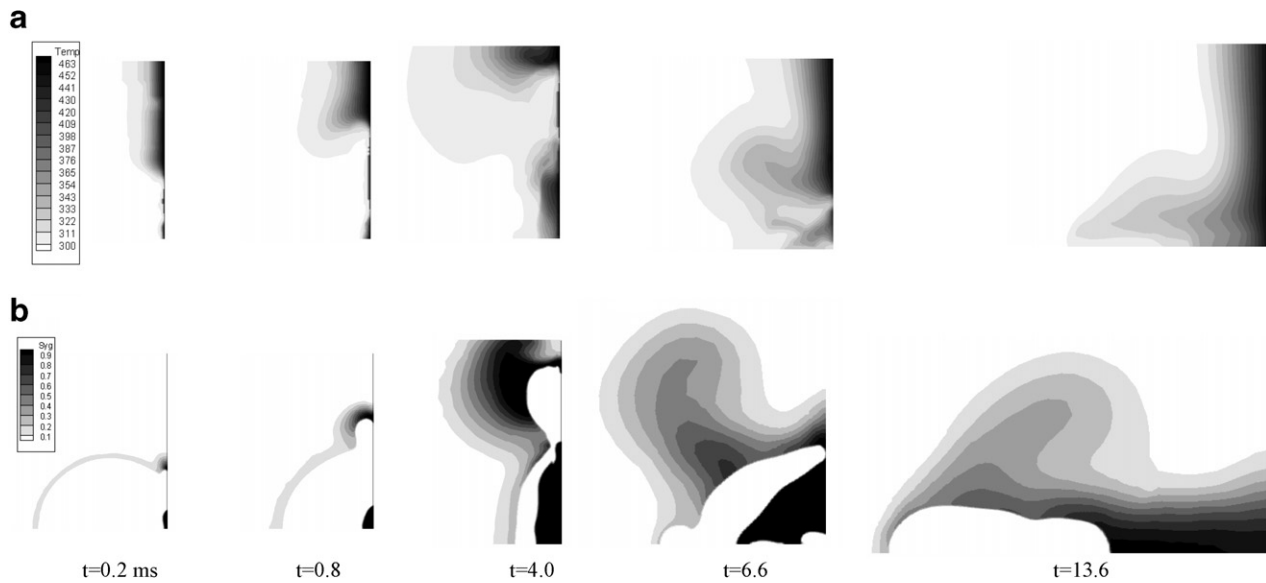
Fig. 6. (a) Temperature filed for case B, and (b) vapor concentration field ($We = 34.52$, $Re = 2156$, $T_w = 190\ °C$, $E_c = 0.034$).

and B, indicating the similarity of the hydrodynamic impingement process at the initial stages of droplet impact, independently of the substrate's temperature. However, at latter times the corresponding pressure rise below the droplet is different. In case B the maximum pressure is much higher than in case A, due to the faster evaporation rate induced by the higher wall temperature.

The time evolution both of temperature and vapor concentration are similar to those of case A, except for the fact that the vapor bubble in this case B is bigger at the same time after impact, than in case A; as a consequence, the temperature diffusion process is more intensive as shown in Fig. 6a and b.

4.1.3. n-Heptane, $T_w = 210\ °C$ (case C)

Case C corresponds to film boiling regime which exists for substrate temperatures above the Leidenfrost point of

vaporization. At this point, the heat flux is minimum and the surface is fully covered by a vapor blanket and heat transfer from the surface to the liquid is only through conduction from this vapor layer. However, as the surface temperature is increased above the Leidenfrost point, radiation through the vapor film becomes significant and the heat flux increases with increasing wall temperature.

Under these conditions no contact of the liquid droplet with the substrate at any time is observed, and as a consequence not only the droplet shape is different from the previous cases, but also the hydrodynamic behavior changes. The predicted hydrodynamic and thermodynamic behavior agrees well both with the corresponding numerical simulation of Harvie and Fletcher [40] and the corresponding experimental data of Qiao and Chandra [23].

Fig. 7a presents a time sequence of predicted droplet shapes of droplet wall collision for case C. As the droplet
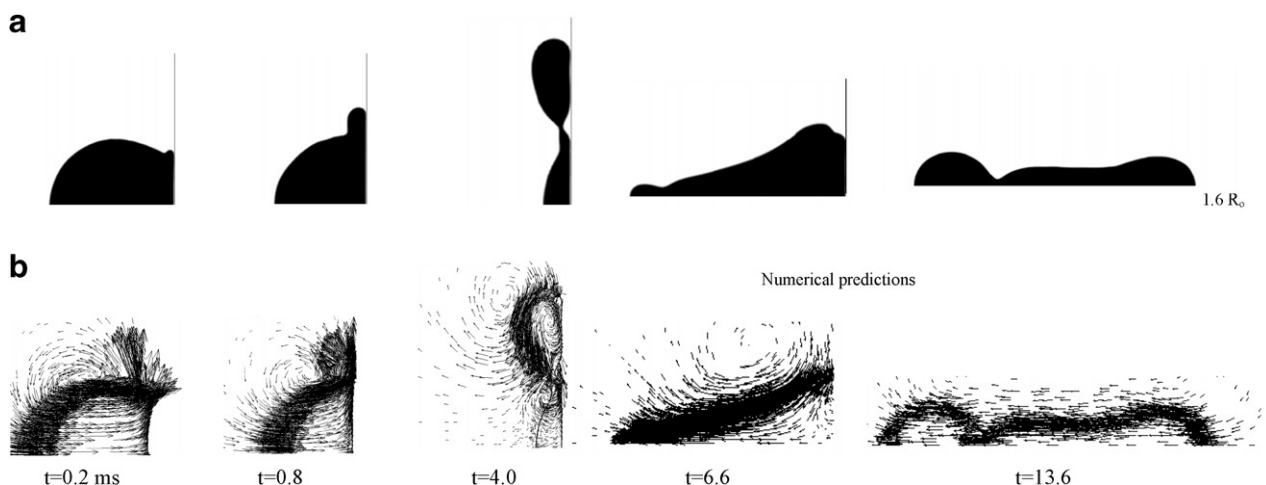
Fig. 7. (a) Droplet shape evolution for case C and (b) vector field ($We = 34.52$, $Re = 2156$, $T_w = 210\ °C$, $E_c = 0.034$).

hits the substrate, spreads onto the vapor film until about time $t = 2.95$ ms and then starts the receding phase, until its complete rebound from the surface; at $t = 13.6$ ms the droplet is levitated around $1.6R_o$ from the wall.

Qiao and Chandra [23] performing this experiment reported that the vapor film between the liquid and the solid phase has a uniform thickness δ, and under this assumption they calculated its value as well as the surface temperature variation using an one-dimensional heat conduction model across the vapor film. This was also confirmed by Harvie and Fletcher [39,40]. The numerical results presented here indicate that this assumption is valid only during the advancing phase of the droplet spreading, but not during the receding phase due to the non uniform distribution of surface tension forces in the region of the interface. As can be seen in Fig. 7a and 8b at $t = 4.0$ ms, there is an increase of the vapor thickness below the neck formed induced by the surface tension coefficient variation with temperature.

Fig. 7b shows the corresponding velocity vector distribution in the computational domain with the time. The maximum of the gas and liquid jetting velocities are approximately 639% and 261% of the droplet impact velocity, respectively. Values of pressure up to approximately 872% of the initial droplet kinetic velocity appear ($C_p = (P - P_{oo}(= 1 \text{ atm}))/(0.5\rho_{liq}U_{oo}^2)$).

In Fig. 8a and b the calculated temperature and vapor fields is presented at the same representative time steps after impact shown previously for cases A and B. As can be seen, in this case C the temperature close to the droplet is lower. This is due to the vapor 'blanket', which reduces the heat flux from the substrate to the droplet, as can be seen in Fig. 8b at $t = 4.0$ ms. At 2.2 ms the vapor height is equal to almost 2% R_o and increases to about 4% R_o and 20% R_o at $t = 2.95$ ms and $t = 4.95$ ms after impact, respectively.

4.2. Characteristics of flow field

4.2.1. Maximum gas–liquid jetting velocity and pressure during the initial stages of the impact

The calculated non-dimensional pressure becomes maximum in case B; this is due to the higher wall temperature compared to case A, but still below the Leidenfrost point. The maximum non-dimensional gas and liquid jetting velocity are of the same order of magnitude for both cases A and B and exhibit the same temporal evolution, accompanied with contact of the droplet with the substrate, while in case C an increase of the maximum gas velocity is predicted with a simultaneous decrease of the maximum liquid velocity. For cases A, B and C, the maximum gas velocity increases until 0.06 ms after impact, whilst the maximum liquid velocity increases until 0.1 ms followed by a decrease.

4.2.2. Spreading rate

Two characteristic lengths are used to quantify droplet spreading: the radius of the wetted area R_{max}, and the droplet height above the surface Z_h, which are defined in Fig. 1b. Normalizing these parameters with the initial droplet radius R_o yields the so-called 'spread factor' and the dimensionless height.

The definition of the 'spread factor' is unambiguous when $T_w < T_{Leid}$, when the droplet wets the surface. In case C, where $T_w > T_{Leid}$ and the droplet no longer wets the surface, this term can be defined as the radius of the flattened area covered by the droplet at the vapor-liquid interface during deformation. Fig. 9 shows the comparison of these parameters with the corresponding experimental data. The numerical predictions are in a good agreement with the experimental data for the maximum spreading radius for cases B and C, and the maximum height for all cases, up to time 7.0 ms after impact. The small differences may
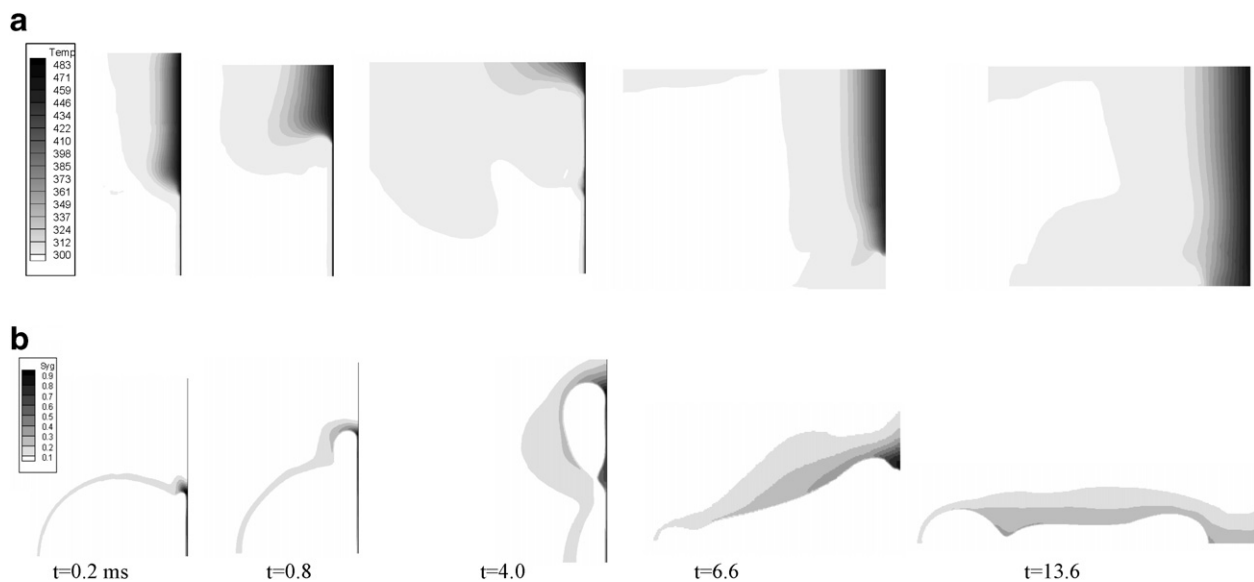
Fig. 8. (a) Temperature filed for case C, and (b) vapor concentration field ($We = 34.52$, $Re = 2156.$, $T_w = 210\ °C$, $E_c = 0.034$).
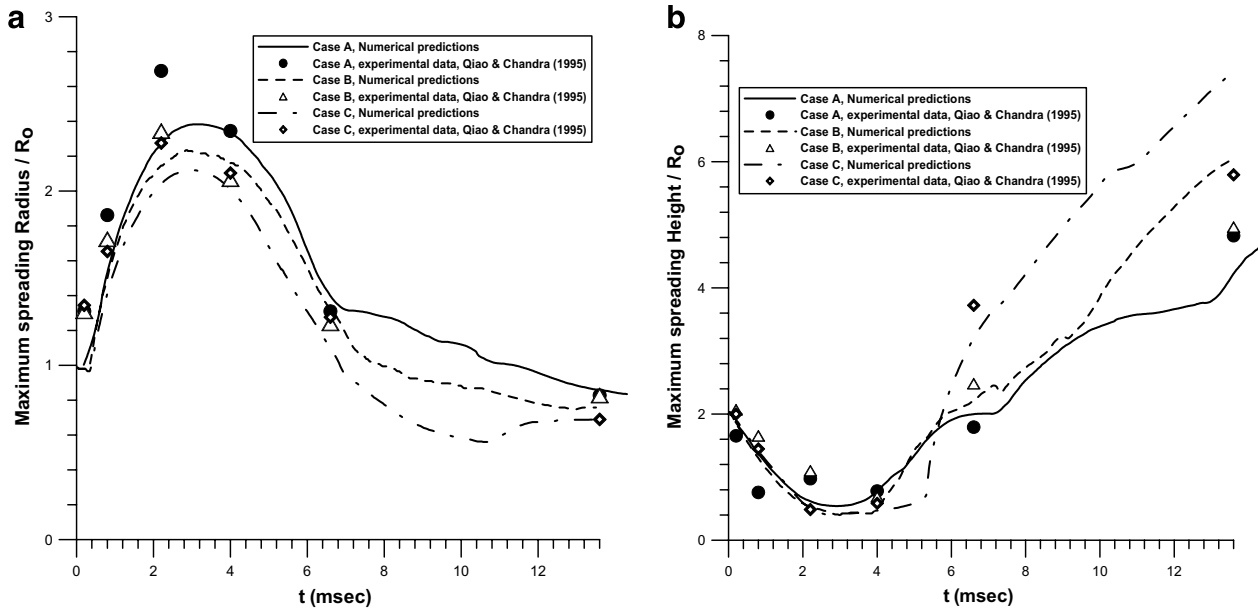
Fig. 9. (a) Maximum non-dimensional radius and (b) maximum non-dimensional height of spreading droplet for cases A, B and C.

be attributed mainly to the fact that in reality the substrate temperature is not constant as cooling takes place during the impact of a liquid droplet. As a result, this changes not only the values of the contact angles and therefore the spreading rate of the droplet, but also the evaporation rate, especially in cases A and B. The effects of the aforementioned parameters are not included in the numerical model.

Moreover we obtained the experimental values of maximum spreading and height by measuring these quantities from the corresponding experimental photos from the paper of Qiao and Chandra [23] and as a result small differences may occur, since these quantities were not reported in their paper.

Both the experimental data and the numerical results show that the 'spread factor' and the height of droplet

are independent of surface temperature in the early period of impact until times $t < 2$ ms, which is also confirmed by Chandra and Avedisian in [5]. Furthermore, the spreading radius of the droplet decreases as the temperature increases, while the spreading height increases.

4.2.3. Heat flux, droplet's temperature and evaporated liquid mass

The average heat flux based on the whole substrate surface (constant reference area) and the average heat flux for the liquid based on the droplet surface which is in contact with the substrate are calculated. This evolution is shown in Fig. 10, where it is found that, for the three cases, the average heat flux from the substrate to the liquid increases as the substrate temperature decreases. This behavior is
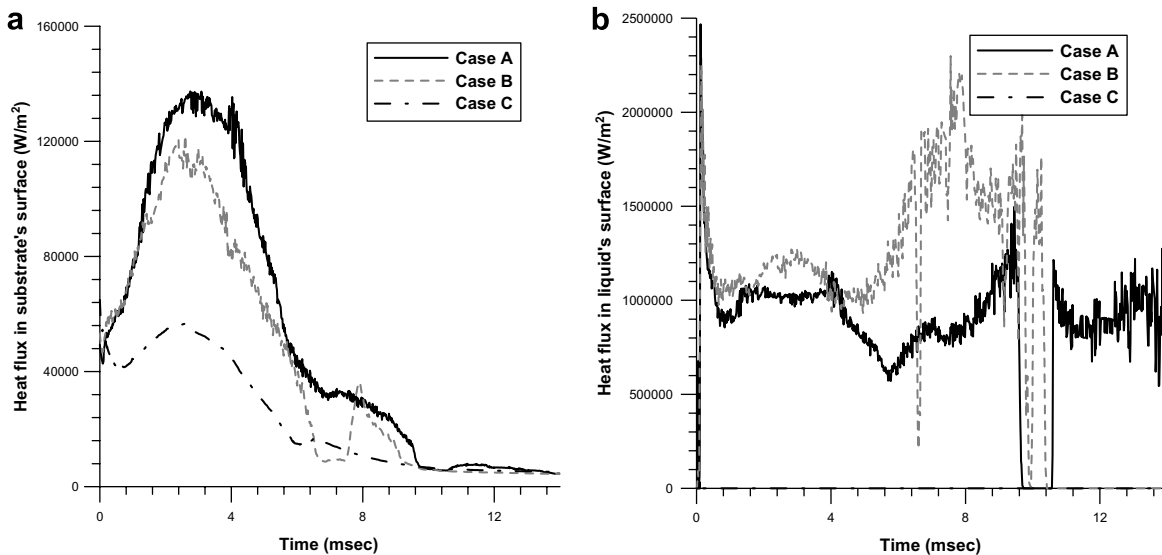
Fig. 10. Time evolution of average heat flux (a) reduced to the substrate's surface and (b) reduced to the liquid phase which is contact with the substrate.

confirmed by the well-known boiling curve in the transition boiling regime, in which the wall heat flux decreases, as the wall superheat $T - T_w$ increases, reaching a minimum heat flux rate at the Leidenfrost point. In Fig. 10a, the maximum value for each case is reached almost at the same time of $t = 3.0$ ms after the impact, which corresponds almost to the start of the receding phase of the droplet on the substrate. When the droplet rebounds, the average heat flux is close to zero. The heat flux, which is perceptible by the liquid surface, is shown in Fig. 10b. This value is higher for case B, than for case A, while in case C is equal to zero, indicating that there is no contact of the liquid with the substrate at any time.

The heat flux that the droplet experiences, inevitably affects its mean temperature; this is plotted in Fig. 11a as a function of time. The mean droplet temperature increases as the wall temperature decreases reaching a value of 80.12 °C in case A and 52.28 °C in case B. In case C, the mean droplet temperature is only 5.2 °C above its initial temperature. In Fig. 11b, the percentage of non-evaporated liquid volume is plotted as a function of time. For case A the increased mean droplet temperature results to the maximum evaporated liquid mass. The corresponding amounts of liquid evaporated until 16 ms after impact are 1.9%, 1.56% and only 0.282%, for cases A, B and C, respectively.

4.2.4. Vapor bubbles

In cases A and B a vapor bubble is formed inside the impacting droplet, which is an important characteristic of the transition boiling regime. The bubble changes in size and shape, until the droplet detaches from the wall. Its volume and the mean pressure (relative to the atmospheric) inside it are presented for cases A and B in Fig. 12a and b, respectively. From Fig. 12a it is evident that during the evolution of the impact process, both for the advancing and the receding phases, the bubble volume increases. This increase is much higher in case B than in case A, since the evaporation rate is greater and more vapor is produced. Especially for case B, the bubble volume almost reaches that of the initial droplet.

The mean pressure within the bubble oscillates around the atmospheric (initial) pressure for case A, while in case B, decreases up to 3 ms, after the impact, and later increases reaching again atmospheric pressure. In case C no vapor bubble is formed and the pressure within the vapor blanket decreases, as shown in Fig. 12b, reaching nearly atmospheric pressure at the latest stages of the process.

4.2.5. Grid independency of the results

For this type of simulation, due to the very fine scales involved one cannot expect to obtain totally mesh independent numerical solution. The results presented have been obtained with four levels of local refinement corresponding to a cell size of $D_o/140$. Note that in the numerical studies reported by Harvie and Fletcher [40] for case C, a cell size of $D_o/50$ has been used. In order to test the grid dependency of the results, cases A and C have been rerun using three and five levels of local refinement corresponding to a cell size of $D_o/70$ and $D_o/280$, respectively.

These results have indicated that the hydrodynamic behavior of the impacting droplet in case A does not change even using three levels of local refinement. However, the thermodynamic behavior changes, as vapor bubbles are not entrapped whilst in case C, vapor blanket is not predicted. Using however five levels of local refinement in cases A and C, both the hydrodynamic and thermodynamic behavior were almost the same with the corresponding ones using four levels of local refinement.
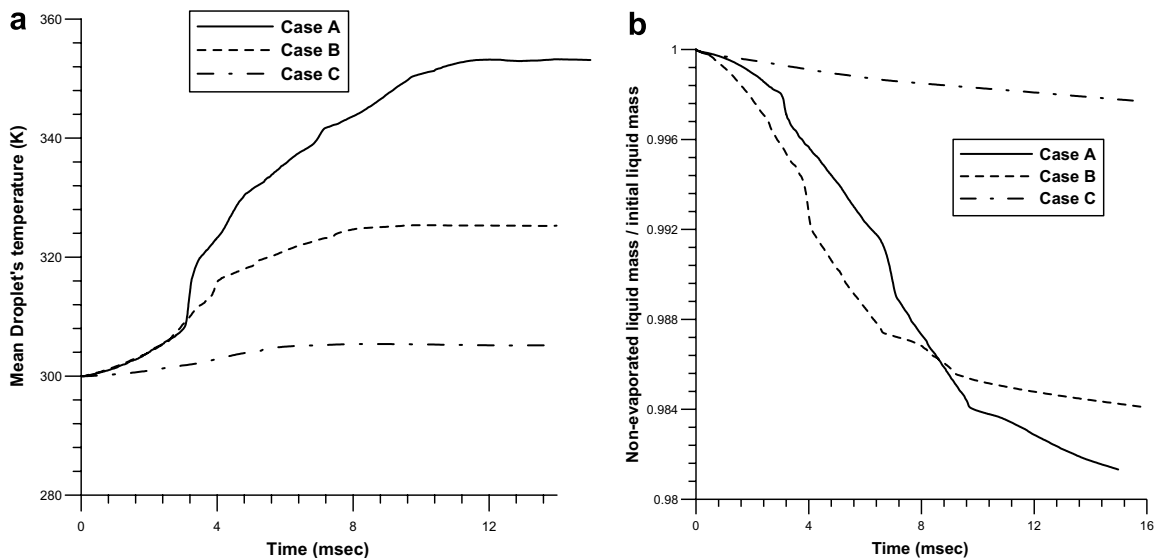
Fig. 11. (a) Mean droplet's temperature and (b) percentage of non-evaporated liquid mass for cases A, B and C.

a

b
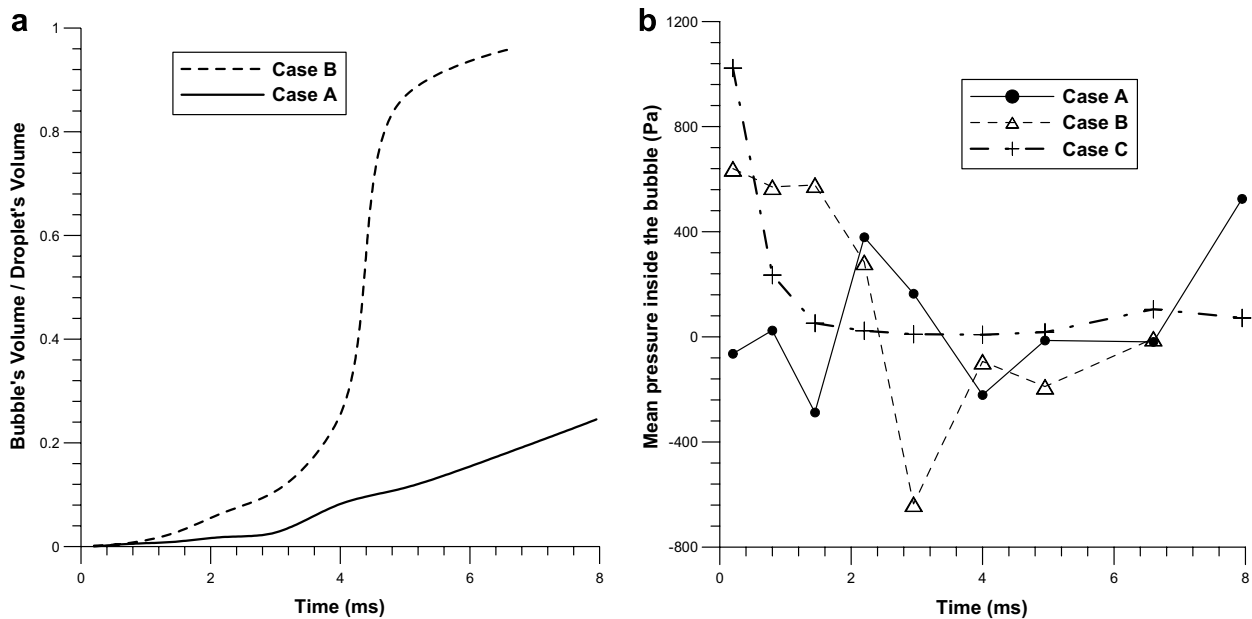
Fig. 12. (a) Time evolution of vapor bubble's volume, dimensioned with the initial droplet's volume and (b) mean pressure inside the bubble, for cases A, B and C.

4.3. Water, $T_w = 180\,°C$ (case D)

The impact of water on a hot aluminum surface under the effect of gravity was investigated experimentally by Bernardin et al. [52]. This case has been simulated in three dimensions and presented here. The Leidenfrost temperature of water is 225 °C [11]. The main differences of this case in respect to the previous ones is that it corresponds to high impact *We* number, and the liquid is water, which has a different behavior from *n*-heptane. The wall temperature of 180 °C corresponds to the midpoint of the boiling transition regime. For $T_w = 180\,°C$ and water, the advancing angle incorporated to the numerical method is equal to 60°.

Fig. 13a presents a time sequence of predicted pictures of the droplet impact for this case D. As the droplet hits the substrate, spreads on it forming a liquid film until about time $t = 4.0$ ms. Since the substrate temperature is below the Leidenfrost temperature and the impact is characterized by a very high *We* number, the droplet experiences contact with the substrate. The spreading film becomes unstable in less than 3 ms, during which vapor is produced, the film becomes highly disturbed but remains intact for the first 3.4 ms, after which it begins to break-up into a large array of droplets which spread radially outwards. The numerical simulation of this phenomenon agrees quite well with the corresponding experimental data [52], at representative times between $t = 0.3$ and 5.0 ms, Fig. 13a. The disintegration of the film into secondary very small droplets is due to two main mechanisms. Firstly, the *We* number of the impact is very high, and even if the surface was cold, the impact would lead to splashing.

Secondly, the vapor bubbles within the spreading liquid film enforce this phenomenon, since the formation of bubbles and the reduction of surface tension in this region induces perturbations in the expanding film, which lead to its disintegration.

At time 3.4 ms after impact, a liquid torus is detached from the expanding film, which doesn't disintegrate into secondary droplets. According to Wachters and Westerling [2] the critical *We* number for torus disintegration is around 80. According to Wu [53] the critical *We* number, above which an expanding torus breaks up, depends on the initial perturbations; in the present case the local *We* number of the torus at this time is calculated to be equal to 40.

Like in the previous cases, the motion of the droplet towards the substrate induces a gas velocity field, in the form of a vortex ring attached to the droplet, $t = 0.3–4.4$ ms, Fig. 14. The values of the maximum gas and liquid jetting velocities are 337% and 278% of the droplet impact velocity, respectively. The mass of film begins to collapse at $t = 4.4$ ms, Fig. 14, as it is evident at the cross-section of slice $Z = 5\%\ Z_{tot}$. This film break-up completes at time 5.0 ms. The predicted mean height of the film at the start of its disintegration is around 5.5% of the initial droplet diameter.

In Fig. 13b and c the temperature and water vapor distributions are presented, respectively, at representative time steps. The temperature of the gas phase is much higher compared to the temperature of the liquid droplet, due to the different specific heat capacity value of the two media; the vapor concentration predicted for case D is smaller compared to that of *n*-heptane for case A, which refers to almost the same substrate temperature of $T_w = 178\,°C$.
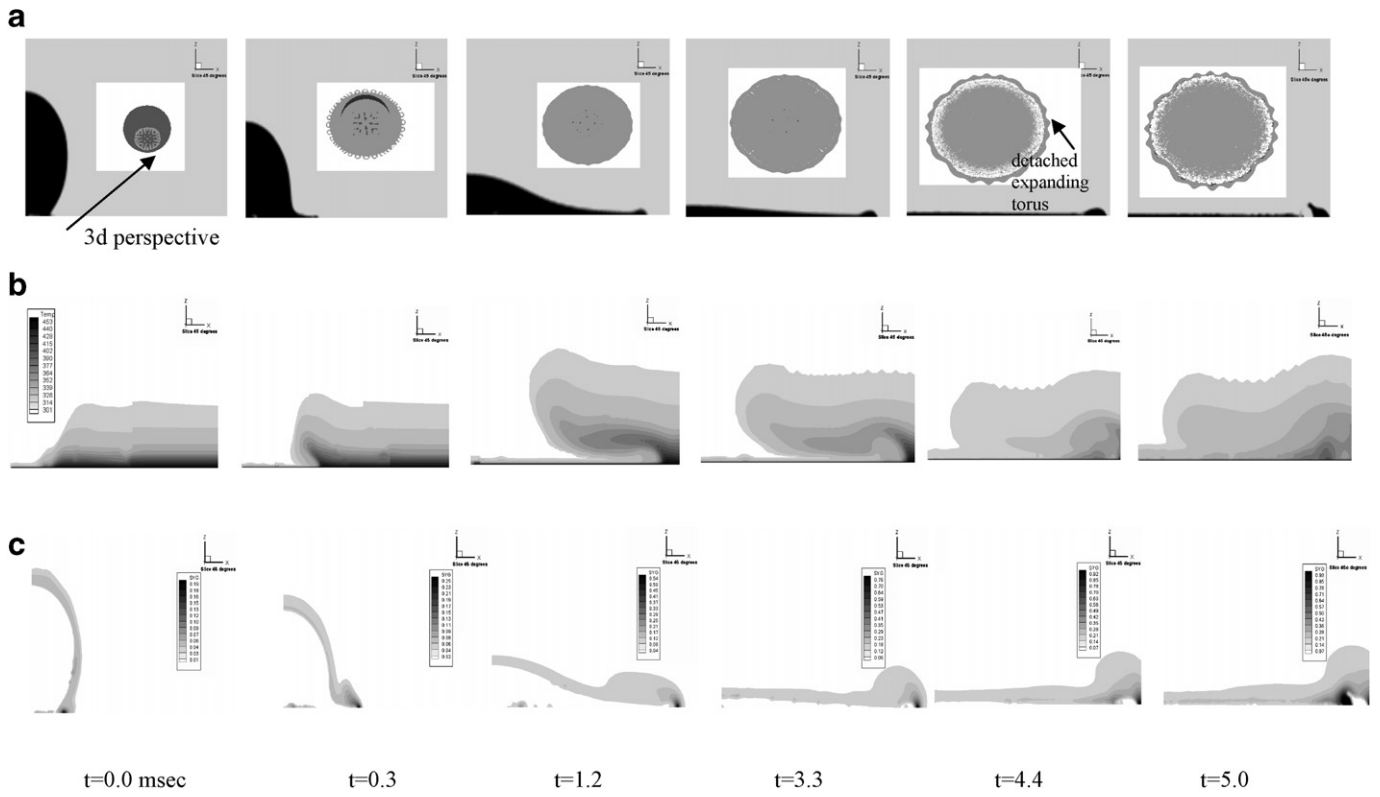
Fig. 13. (a) Droplet shape evolution for case D at vertical slices (45°), (b) corresponding temperature field and (c) corresponding vapor filed ($We = 222$, $Re = 7639$, $T_w = 180 °C$, $B_o = 1.19$, $E_c = 0.06$).
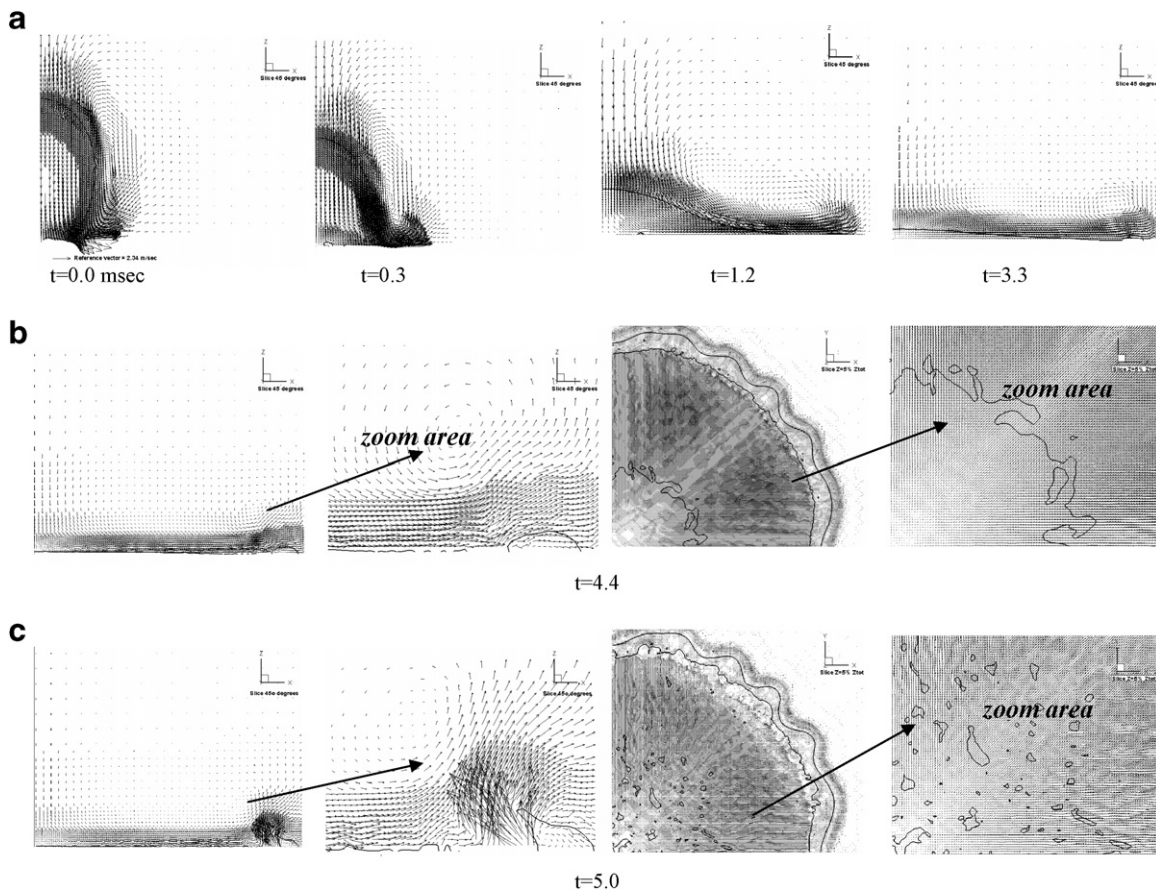
Fig. 14. Vector field for case D at vertical (45°) and horizontal slices ($Z = 5\% Z_{tot}$) ($We = 222$, $Re = 7639$, $T_w = 180 °C$, $B_o = 1.19$, $E_c = 0.06$).
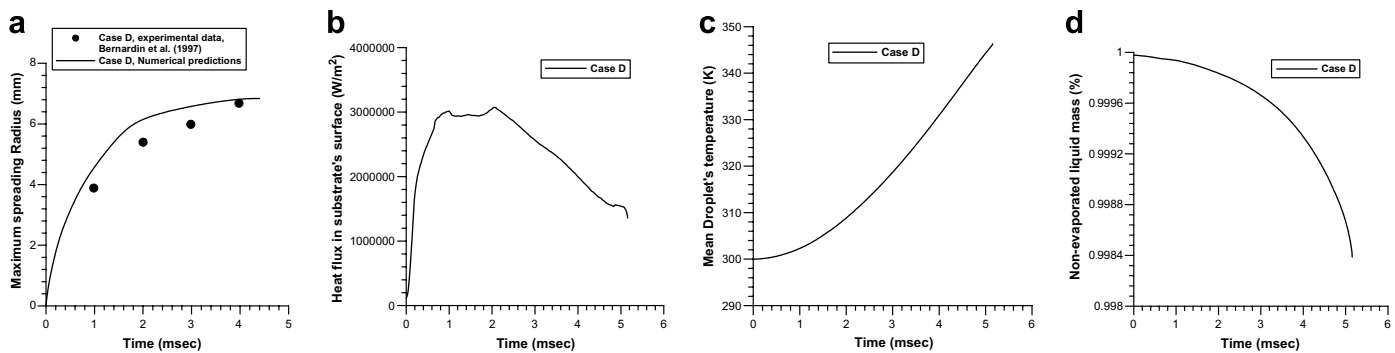
Fig. 15. (a) Maximum radius, (b) time evolution of average heat flux from the substrate to the liquid phase reduced to the substrate's surface, (c) mean droplet temperature, (d) percentage of non-evaporated liquid mass for case D ($We = 222$, $Re = 7639$, $T_w = 180\,°C$, $B_o = 1.19$, $E_c = 0.06$).

Fig. 15a shows the evolution of the spreading radius for case D, with the corresponding experimental data, where a good agreement is found. The liquid spreading for case D is faster compared to cases A, B and C, since the *We* number of impact for this case is much bigger.

4.3.1. Heat flux, droplet's temperature and evaporated liquid mass

The average heat flux from the substrate to the liquid phase per substrate's surface area is calculated and plotted as function of time in Fig. 15b. The average heat flux is higher for water than for *n*-heptane and as a result, it affects its mean temperature which reaches a maximum value of 73.32 °C, as shown in Fig. 15c in contrast to *n*-heptane, for which a maximum temperature of 58.93 °C was predicted at 5.16 ms after impact. Finally the percentage of droplet liquid mass vaporized during the impact is 0.16% at 5 ms as can be seen in Fig. 15d. This percentage is less than the corresponding value predicted for h-heptane for cases A and B.

5. Conclusions

The flow development during normal impingement of droplets onto a hot wall was numerically studied using a finite volume Navier–Stokes equations flow solver incorporating the Volume of Fluid (VOF) methodology. Use of an evaporation model predicting the vapor produced during impact, together with numerical solution of two additional transport equations for the temperature and vapor concentration fields has allowed estimations of the coupled hydrodynamic and thermodynamic process. The numerical model utilizes an adaptive local grid refinement technique at the liquid–gas interface which has allowed prediction of the flow development taking place during droplet impingement on a heated surface with temperature below or above the Leidenfrost point. Droplet levitation from the surface was calculated without any 'a priori' assumption for the vapor layer height forming between the liquid and the wall. For high impact *We* number but on a surface with temperature below Leidenfrost, the splashing of the liquid associated with the formation of a ring detached from the spreading lamella is predicted, while the remaining film becomes highly disturbed and breaks into a large array of droplets. Moreover, formation of vapor bubbles within the bulk of the liquid was predicted while its volume was calculated transiently during the numerical solution.

The numerical results agree reasonably well with the experimental data, both qualitatively, in terms of the liquid droplet shape deformation process and quantitative, in terms of the spreading rate and height. Information regarding the temperature, concentration and pressure fields developing at scales that is not possible to estimate experimentally has been provided. Additional information for averaged or point properties, such as the total vapor bubble entrapment, the maximum droplet deformation, and the air and liquid jetting velocities have been reported.

References

[1] J.G. Leidenfrost, De aquae communis nonullis qualitatibus tractatus – on the fixation of water in divers fire. A tract about some qualities of common water (translated into English by Wares C), Int. J. Heat Mass Transfer 9 (1966) 1153–1166.

[2] L.H.J. Wachters, N.A. Westerling, The heat transfer from a hot wall to impinging water drops in the spheroidal state, Chem. Eng. Sci. 21 (1966) 1047–1056.

[3] F. Akao, K. Araki, S. Mori, A. Moriyama, Deformation behaviors of a liquid droplet impinging onto hot metal surface, Trans. ISR 20 (1980) 737–743.

[4] T.Y. Xiong, M.C. Yuen, Evaporation of a liquid droplet on a hot plate, Int. J. Heat Mass Transfer 34 (7) (1991) 1881–1894.

[5] S. Chandra, C.T. Avedisian, On the collision of a droplet with a solid surface, Proc. R. Soc. Lond. Ser. A 432 (1991) 13–41.

[6] S. Chandra, C.T. Avedisian, Observations of droplet impingement on a ceramic porous surface, Int. J. Heat Mass Transfer 35-10 (1992) 2377–2388.

[7] J.D. Naber, P.V. Farell, Hydrodynamics of droplet impingement on a heated surface. SAE technical paper, 930919, 1993.

[8] K. Anders, N. Roth, A. Frohn, The velocity change of ethanol droplets during collision with a wall analyzed by image processing, Exp. Fluids 15 (1993) 91–96.

[9] Y.S. Ko, S.H. Chung, An experiment on the breakup of impinging droplets on a hot surface, Exp. Fluids 21 (1996) 118–123.

[10] S. Manzello, J. Yang, On the collision dynamics of a water droplet containing an additive on a heated solid surface, Proc. R. Soc. Lond. A. 458 (2002) 2417–2444.

[11] J.D. Bernardin, C.J. Stebbins, I. Mudawar, Effects of surface roughness on water droplet impact history and heat transfer regimes, Int. J. Heat Mass Transfer 40 (1) (1997) 73–88.

[12] J.D. Bernardin, I. Mudawar, C.B. Walsh, E.I. Franses, Contact angle temperature dependence for water droplets on practical aluminium surfaces, Int. J. Heat Mass Transfer 40 (5) (1997) 1017–1033.

[13] M. Cumo, G.E. Farello, G. Ferrari, Notes on droplet heat transfer, Chem. Eng. Prog. Symp. Ser. 65 (1969) 175–187.

[14] K.J. Baumeister, R.E. Henry, F.F. Simon, Role of the surface in the measurement of the Leidenfrost temperature, in: A.E. Bergles, R.L. Webb (Eds.), Augmentation of Convective Heat and Mass Transfer, ASME, New York, 1970, pp. 91–101.

[15] S. Nishio, M. Hirata, Study on the Leidenfrost temperature (2nd report, behavior of liquid–solid surface contact and Leidenfrost temperature), Trans. JSME 44 (1977) 1335–1346.

[16] C.T. Avedisian, J. Koplik, Leidenfrost boiling of methanol droplets on hot porous/ceramic surfaces, Int. J. Heat Mass Transfer 30 (1987) 379–393.

[17] O.G. Engel, Waterdrop collisions with solid surfaces, J. Res. NBS 54 (1955) 281–298.

[18] E.N. Ganic, W.M. Rohsenow, Dispersed flow heat transfer, Int. J. Heat Mass Transfer 20 (1977) 855–866.

[19] H. Fujimoto, N. Hatta, Deformation and rebounding processes of a water droplet impinging on a flat surface above Leidenfrost temperature, Trans. ASME, J. Fluids Eng. 118 (1996) 142–149.

[20] N. Hatta, H. Fujimoto, K. Kinoshita, H. Takuda, Experimental study of deformation mechanism of a water droplet impinging on hot metallic surfaces above the Leidenfrost temperature, Trans. ASME, J. Fluids Eng. 119 (1997) 692–699.

[21] S. Chandra, M. Di Marzo, Y.M. Qiao, P. Tartarini, Effect of liquid–solid contact angle on droplet evaporation, Fire Safety J. 27 (1996) 141–158.

[22] R. Siegel, Effects of reduced gravity on heat transfer, Adv. Heat Transfer 4 (1967) 143–229.

[23] Y.M. Qiao, S. Chandra, Boiling of droplets on a hot surface in low gravity, Int. J. Heat Mass Transfer 39 (7) (1996) 1379–1393.

[24] B.S. Gottfried, C.J. Lee, K.J. Bell, The Leidenfrost phenomenon: film boiling of liquid droplets on a flat plate, Int. J. Heat Mass Transfer 9 (1966) 1167–1187.

[25] L.H.J. Wachters, L. Smulders, J.R. Vermeulen, H.C. Kleiweg, The heat transfer from a hot wall to impinging mist droplets in the spheroidal state, Chem. Eng. Sci. 21 (1966) 1231–1238.

[26] T.K. Nguyen, C.T. Avedisian, Numerical solution for film evaporation of a spherical droplet on an isothermal and adiabatic surface, Int. J. Heat Mass Transfer 30 (1987) 1497–1509.

[27] S. Zhang, G. Gogos, Film evaporation of a spherical droplet over a hot surface: fluid mechanics and heat/mass analysis, J. Fluid Mech. 222 (1991) 543–563.

[28] M. Pasandideh-Fard, R. Bhola, S. Chandra, J. Mostaghimi, Deposition of tin droplets on a steel plate: simulations and experiments, Int. J. Heat Mass Transfer 41 (1998) 2929–2945.

[29] M. Pasandideh-Fard, S.D. Aziz, S. Chandra, J. Mostaghimi, Cooling effectiveness of a water drop impinging on a hot surface, Int. J. Heat Fluid Flow 22 (2001) 201–210.

[30] M. Pasandideh-Fard, S. Chandra, J. Mostaghimi, A three-dimensional model of droplet impact and solidification, Int. J. Heat Mass Transfer 45 (2002) 2229–2242.

[31] M. Bussmann, J. Mostaghimi, S. Chandra, On a three-dimensional volume tracking model of a droplet impact, Phys. Fluids 11 (1999) 1406–1417.

[32] L.L. Zheng, H. Zhang, An adaptive level set method for moving-boundary problems: application to droplet spreading and solidification, Numer. Heat Transfer Part B 37 (2000) 437–454.

[33] Ghafouri-Azar, S. Shakeri, S. Chandra, J. Mostaghimi, Interactions between molten droplets impinging on a solid surface, Int. J. Heat Mass Transfer 46 (2003) 1395–1407.

[34] Z. Zhao, D. Poulikakos, Heat transfer and fluid dynamics during the collision of a liquid droplet on a substrate – I. Modeling, Int. J. Heat Mass Transfer 39 (13) (1996) 2771–2789.

[35] Z. Zhao, D. Poulikakos, Heat transfer and fluid dynamics during the collision of a liquid droplet on a substrate – II. Experiments, Int. J. Heat Mass Transfer 39 (13) (1996) 2791–2802.

[36] J.M. Waldvogel, D. Poulikakos, Solidification phenomena in picoliter size solder droplet deposition on a composite substrate, Int. J. Heat Mass Transfer 40 (2) (1997) 295–309.

[37] V. Butty, D. Poulikakos, J. Giannakouros, Three dimensional presolidification heat transfer and fluid dynamics in molten micro-droplet deposition, Int. J. Heat Fluid Flow 23 (2002) 232–241.

[38] D.J.E. Harvie, D.F. Fletcher, A simple kinetic theory treatment of volatile liquid–gas interfaces, Trans. ASME 123 (2001) 486–491.

[39] D.J.E. Harvie, D.F. Fletcher, A hydrodynamic and thermodynamic simulation of droplet impacts on hot surfaces, Part I: theoretical model, Int. J. Heat Mass Transfer 44 (2001) 2633–2642.

[40] D.J.E. Harvie, D.F. Fletcher, A hydrodynamic and thermodynamic simulation of droplet impacts on hot surfaces, Part II: validation and applications, Int. J. Heat Mass Transfer 44 (2001) 2643–2659.

[41] C.W. Hirt, B.D. Nichols, Volume of fluid (VOF) method for the dynamics of free boundaries, J. Comput. Phys. 39 (1981) 201–225.

[42] N. Nikolopoulos, A. Theodorakakos, G. Bergeles, Normal impingement onto a wall film: a numerical investigation, Int. J. Heat Fluid Flow 26 (2005) 119–132.

[43] A. Theodorakakos, G. Bergeles, Simulation of sharp gas–liquid interface using VOF method and adaptive grid local refinement around the interface, Int. J. Numer. Meth. Fluids 45 (2004) 421–439.

[44] O. Ubbink, R.I. Issa, A method for capturing sharp fluid interfaces on arbitrary meshes, J. Comput. Phys. 153 (1) (1999) 26–50.

[45] H. Jasak, Error analysis and estimation for finite volume method with applications to fluid flows, Ph.D. Thesis, Department of Mechanical Engineering, Imperial College of Science, Technology & Medicine, University of London, 1996.

[46] I. Langmuir, The dissociation of hydrogen into atoms Part II, J. Am. Chem. Soc. 37 (1915) 417.

[47] R.W. Schrage, A Theoretical Study of Interphase Mass Transfer, Columbia University Press, New York, 1953.

[48] J. Straub, M. Zell, B. Vogel, Pool boiling in a reduced gravity field, in: Proceedings of the Nineth International Heat Transfer Conference, vol. 1, 1990, pp. 91–112.

[49] T. Oka, Y. Abe, K. Tanaka, Y.II. Mori, A. Nagashima, Observational study of pool boiling under microgravity, JSME Int. J. 35 (1992) 280–286.

[50] J.S. Ervin, H. Metre, R.B. Keller, K. Kirk, Transient pool boiling in microgravity, Int. J. Heat Mass Transfer 35 (1992) 659–674.

[51] S. Nishio, M. Hirata, in: Proceedings of the 6th International Heat Transfer Conference, Toronto, vol. 1, 1978, pp. 245–250.

[52] J.D. Bernardin, C.J. Stebbins, I. Mudawar, Mapping of impact and heat transfer regimes of water drops impinging on a polished surface, Int. J. Heat Mass Transfer 40 (2) (1997) 73–88.

[53] Z.N. Wu, Approximate critical *We* number for the breakup of an expanding torus, Acta Mech. 166 (2003) 247–267.